Free and Bound Capillary Waves as Microwave Scatterers: Laboratory Studies

Anatol D. Rozenberg, Michael J. Ritter, W. Kendall Melville, Christopher C. Gottschall, and Andre V. Smirnov

***Abstract*— Laboratory measurements of the fine space-time structure of short gravity-capillary waves, as well as Ku-band scattering at grazing and moderate incidence from wind waves in the large Delft Hydraulics Laboratory wind-wave channel are presented. This study was stimulated by the need to verify the processes that significantly contribute to scattering at grazing and moderate incidence. A scanning laser slope gauge was used for measuring capillary waves from 2-mm to 2-cm wavelengths and frequencies ranging up to 100 Hz. A dual-polarized (vertical, VV, and horizontal, HH), coherent, pulsed Ku-band scatterometer with good temporal resolution (3 ns) was used to obtain simultaneous Doppler spectra and the absolute cross section of scattered signals for grazing angles 6 and 25° and for winds in the range 2.5–12.5 m/s.**

Two-dimensional (2-D) filtering and bispectral analyses were used to separate and study the influence of free and bound surface waves. The results of this study demonstrate that the frequency-wavenumber spectra of capillary waves consist of two parts. The first corresponds to free capillary waves, which satisfy the dispersion relationship. The second corresponds to bound parasitic capillary waves, which are located near the crests of steep wind waves. The phase velocity of these capillary waves is approximately equal to the phase velocity of the steep waves.

Measurements of the Doppler frequency of the scattered signals show that the Doppler spectra also have a bimodal structure. While the first low-frequency part of the spectrum corresponds to the Bragg scattering from the free capillary waves, the high-frequency part is associated with Bragg scattering from the bound capillary waves on the crests of the steep waves. This type of scattering is predominant for the upwind direction of illumination (especially for HH-polarization).

***Index Terms*— Bragg scattering, electromagnetic scattering from rough surfaces, remote sensing.**

I. Introduction

THIS STUDY is a continuation of previous laboratory measurements at the Scripps Institution of Oceanography (SIO) wind-wave tank of dual-polarized Ku-band scattering at grazing incidence [14], [15]. Two remarkable features were found during that study which were based on a comparison between measured Doppler frequency of the scattered signal and the phase velocity of possible scatterers.

Manuscript received October 6, 1997; revised June 17, 1998. This work was supported by ONR (Remote Sensing) and NSF (Physical Oceanography) and from a joint NOAA/DOD-Advanced Sensor Application Program.

A. D. Rozenberg, M. J. Ritter, and W. K. Melville are with the Scripps Institution of Oceanography, University of California, San Diego, La Jolla, CA 92093-0230 USA (e-mail: kmelville@ucsd.edu).

C. C. Gottschall and A. V. Smirnov are with the Environmental Technology Laboratory, National Oceanographic and Atmospheric Administration, Boulder, CO 80303-3328 USA.

Publisher Item Identifier S 0196-2892(99)01973-7.

Initially, the study showed that all data could be separated into two groups. The first corresponded to HH scattering in the upwind look direction and was clearly associated with scattering from features of the surface traveling at the phase speed of the dominant gravity wind-waves. The second corresponded to HH scattering in the downwind look direction and all VV scattering, and it was consistent with Bragg scattering from the capillary wind waves. Second, modulation of the scattered signal by longer (3-s period) mechanically generated waves showed significant dependence of the modulation parameters not on the long wave amplitude only, but on wind speed, especially for the waves in the first group.

In some cases, these features can be considered as indirect evidence of a scattering process that is more complicated than the simple composite (two-scale) model [19]. Many authors have expressed doubts about the comprehensiveness of the composite model, which assumes Bragg scattering from small free gravity-capillary waves riding on longer waves. Most have associated the scattering phenomenon with the appearance of patches of large slope on the forward face of the dominant wind waves.

One of the most likely scenarios for these patches could be the so-called parasitic or bound gravity-capillary waves. Generated by steep gravity waves, they have been theoretically examined by Longuet–Higgins [10] (1993) and most recently by Fedorov and Melville (1998). Surprisingly, little information is available on these waves, particularly, experimental data. Regular bound waves, generated by short steep gravity waves in a frequency range from 3 to 6 Hz have been studied experimentally [1], [13], [16], [20], [Fedorov *et al.*, 1998].

The difficulties of studying bound waves generated by steep wind waves are clear. The wave field in this case should be presented as a superposition of the free and bound waves with an approximately similar spatial scale, even though their frequencies are quite different. The strong nonlinearity of the bound waves makes the usual spectral analysis inefficient and requires additional methods of analysis. Here, two-dimensional (2-D) frequency-wavenumber spectral analysis is used to separate the two types of waves by their phase velocities, and bispectral analysis is used to identify nonlinear effects.

The development of the scanning laser slope gauge (SLSG) in the last decade has opened new opportunities for studying bound waves and their influence on scattering phenomena. Kwoh and Lake [8] simultaneously used SLSG and an X-band CW scatterometer in a laboratory wave tank to study scattering from gently breaking mechanically generated 2.5-Hz waves. The presence of parasitic short waves at the moment

of breaking, consistent with the measured scattering, was mentioned. A nonscanning mode of SLSG enabled only time series of the surface slope to be obtained.

Trizna *et al.* [17], [18] used the SLSG and a dual-polarized, X-band scatterometer with excellent spatial resolution (10 cm) to study sea spikes in scattering by wind waves imposed on 1-Hz mechanically generated waves in a wind-wave channel. Non-Bragg scattering for some parts of the surface was observed. Unfortunately, the SLSG data were only used for illustrative purposes.

Keller *et al.* [6] provided simultaneous measurements in a wind-wave tank with X and Ka-band scatterometers and an optical system. Their optical device, like that developed by Keller and Gotwals [6] and Jaehne and Riemer [9], transformed an image of the wave surface into a 2-D field of the upwind/downwind slope component. While the presence of parasitic capillary waves on the images was mentioned, only along-tank integrated wavenumber slope spectra (for both free and parasitic waves) were considered.

While many studies have drawn attention to parasitic capillary waves, we are not aware of any attempts to isolate them to directly study their role in surface scattering. It may be that the optical instrumentation did not have the required temporal and spatial resolution to separate the free and bound waves according to their different phase velocities.

In [11], an attempt at such a separation was made. The 2-D wavenumber-frequency spectrum for the slope field of the short wind waves measured by a SLSG demonstrated the presence of bound waves.

In recent studies [4], [5], three-dimensional (3-D) spectra of the slope field of short wind waves were examined. The presence of "free" and "generalized bound waves" was observed, but limitations on the temporal resolution (30 ms) made it difficult to properly separate free and bound waves.

As an extension of the work of [11], in the present study, we try to clarify the nature of the different scatters and focus, at first, on the fine space-time structure of wind waves responsible for scattering, especially bound waves. The bound capillary waves may provide a significant contribution to scattering under typical conditions.

The second aim of this study is associated with the use of a longer wind-wave channel with 80-m fetch. Our previous study in the SIO wind-wave channel with an 11-m fetch and, accordingly, a small energy density of the dominant waves corresponds, as will be shown later, to simpler scattering conditions. The transition to the longer channel with more complex and realistic scattering conditions is the next essential step toward field conditions. To emphasize the influence of the fetch on scattering, comparison of the results for both channels will be presented.

II. Experimental Methods

A. Wave Tank

The facility used to obtain these data is the Delft Hydraulics Laboratory wind-wave channel [Fig. 1(a)]. The channel is 100 m long, 8 m wide, and 2.4 m high, increasing to 2.65 m in the working section. The wave tank was filled with fresh water to a depth of 0.7 m. The scatterometer is mounted in different upwind/downwind positions to obtain a common footprint with the scanning laser slope gauge. The instrumentation is located at a fetch of 85 m upwind from the fan screens. At the downwind end of the channel, a beach dissipates the incoming waves.

B. Microwave System

A coherent 14-GHz ($\lambda = 2.1$ cm), dual-polarized, pulsed system is used for obtaining the amplitude and phase of the scattered signal. The scatterometer has two slightly different ($\Delta F = 240$ MHz) transmitter frequencies for obtaining simultaneous VV- and HH-polarized signals. Two short-pulse amplitude modulators provided 3-ns modulation of the transmitted signal (45-cm spatial resolution). The scatterometer was described in detail in [14]. A two-channel Stanford Research System Model SR250 Fast Gated Integrator and Boxcar Averager is used for converting the short-pulse signal of bandwidth 0–240 MHz to a low-frequency (0–3.75 kHz) analog signal for the VV and HH channels. The electronics is mounted directly on the antenna array. The transmitting and receiving antennas are two 20-cm diameter horns with a one-way, 3-dB beam width of approximately 6.7°. The antennas were fixed under the wind-tunnel roof, 40–70 cm above the water surface, and centered in the cross-tank direction. The grazing angle could be varied from 6 to 25°, and the antennas could be positioned to give either an upwind or downwind direction of illumination. The scatterometer was calibrated using a swinging 6.5-cm diameter aluminum sphere at a distance of 3.5 m. The calibration curves are equal for both channels with an error of ± 1 dB.

C. Scanning Laser Slope Gauge

A one-dimensional (1-D) SLSG was designed for measuring the fine space-time structure of the high wavenumber wind waves. The slope measurement is based on the refraction of a light-ray incident upon the water–air interface from below. The surface slope (the angle α between normal to surface and vertical incident ray) can be found in accordance with Snell's law and position geometry as

$$\alpha = \arctan\left(\frac{\frac{n_a}{n_w}\cdot\frac{x}{h}}{1-\frac{n_a}{n_w}}\right) \tag{1}$$

where n is the refraction index, subscripts w and a denote water and air, respectively, and x is the horizontal ray deflection onto a screen located at a distance h from the mean water surface.

The SLSG consists of an underwater laser and scanner assembly, the position-sensor assembly above the water surface, and a CCX650 Scanner Control Amplifier. The schematic of the SLSG is shown in Fig. 1(c). The 3-mW, 617-nm laser diode LPM02 and scanner with a flat glass mirror were housed in a waterproof enclosure 80 cm beneath the surface. The CCX650 Scanner Control Amplifier scanned the mirror at 200 Hz (giving a 8–10-cm long line on the water surface in the wave propagation direction) and a trigger pulse for

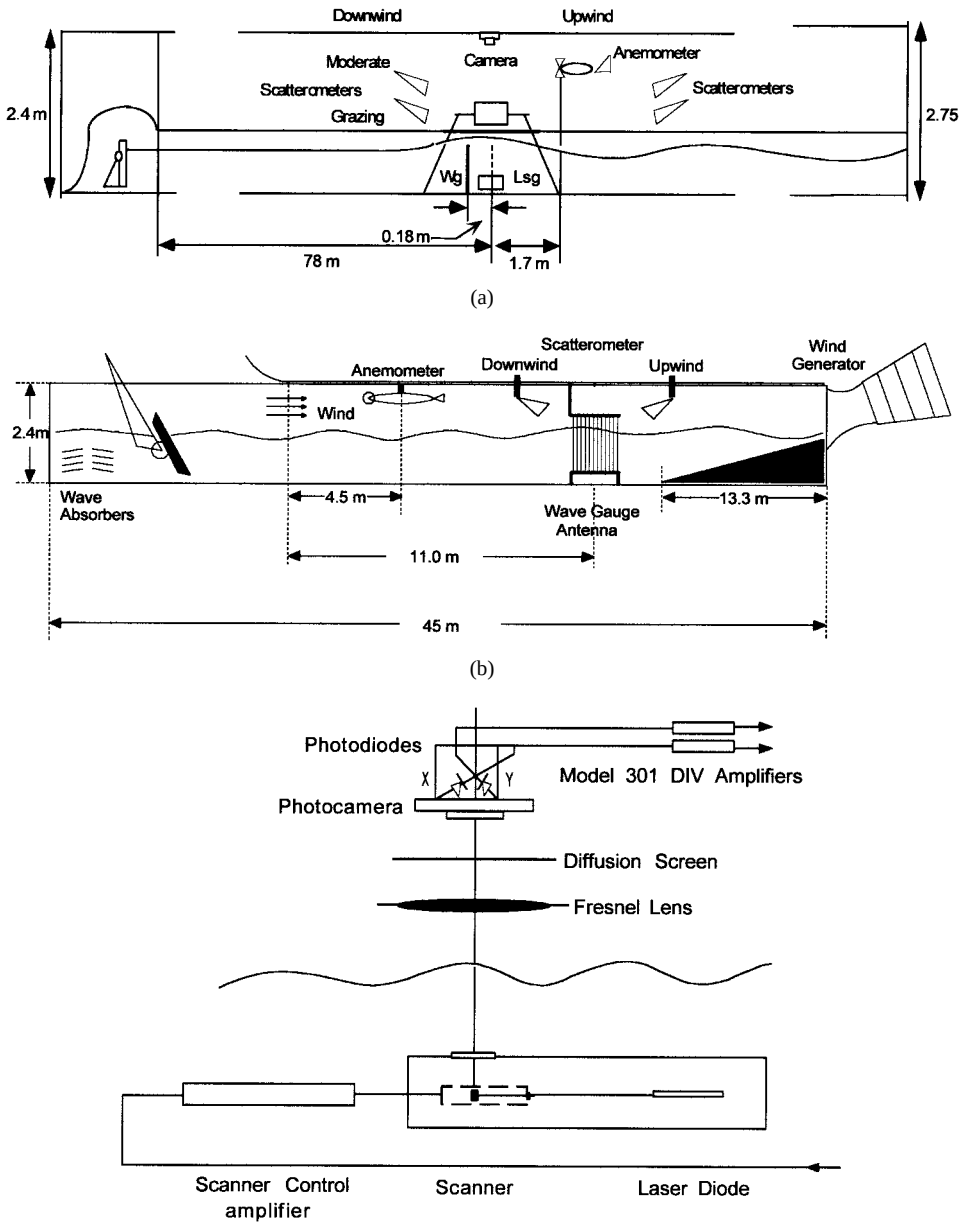

Fig. 1. Schematics of the laboratory wind-wave channels at (a) Delft Hydraulics, (b) SIO, and (c) the scanning laser slope gauge.

image synchronization. The position-sensor assembly included a 22-cm diameter Fresnel lens, an LCD diffusion screen, a red bandpass interference filter, and an imaging lens focusing onto an SC-10 position photodiode. After preprocessing by the 301 DIV Amplifier, and synchronizing with the trigger, the position signal from the photodiode is sampled at 50 kHz with a two-channel A/D board. The 50-kHz sampling rate allowed us to obtain one 64 $\times$ 200 pixel space-time image every second. The usual duration of one record was 0.5–1.5 min. Dynamic calibrations were performed using a transparent cylindrical lens floating on the water surface.

D. Supporting Instrumentation

The surface displacement field was measured with a 0.1-mm diameter nichrome resistance wire wave gauge connected to a Danish Hydraulic Institute Model 80-74G amplifier. It was mounted 18 cm upstream of the scanning laser slope gauge. The wind speed at the center line was measured 50 cm above the mean water level with a propeller-type (Young Model 05 305) anemometer that was calibrated with a Pitot-static tube. Air and water temperatures were measured with a standard mercury thermometer.

E. Data Acquisition

Data were acquired on a 486 PC equipped with two Metrabyte DAS16 cards (12-bit, eight differential channels) for analog-to-digital conversion. Two modes of operation with different sampling rates were used. Four analog signals (VV and HH scatterometer outputs, the SLSG in stationary mode, and wave gauge) were sampled at a frequency of 4 kHz (1 kHz

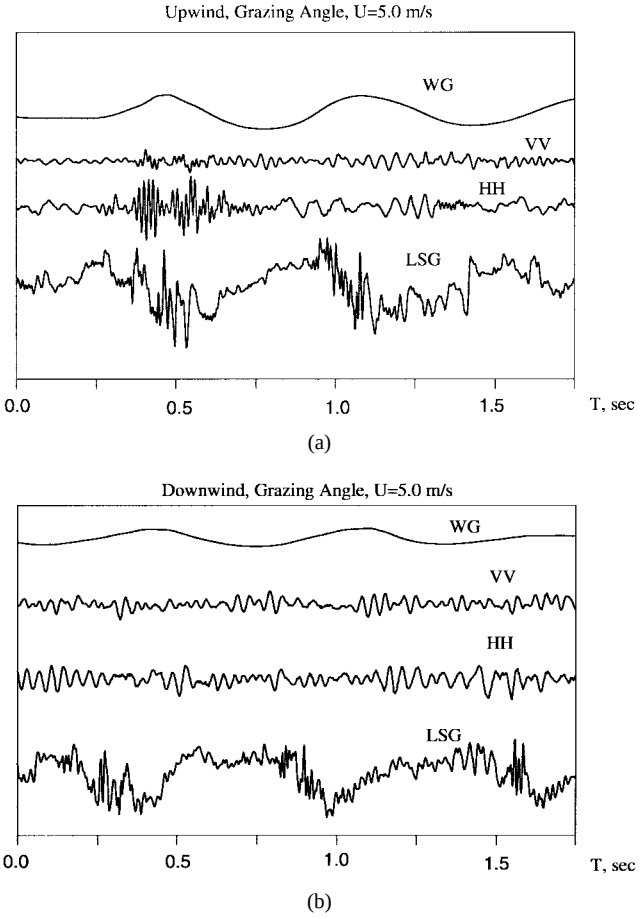

Fig. 2. Time series for the wave height gauge, VV and HH scattered signals, and laser slope gauge for (a) upwind and (b) downwind directions of illumination at Delft for a 6° grazing angle and wind speed 5 m/s. While the wave height and slope time series are similar for both cases, the spiky high-frequency patches on the scattered signal time-series occur only for the upwind direction (especially for HH). Note, the wave gauge is 18-cm upstream of laser slope gauge. Arbitrary linear vertical scales.

per channel) for 5 min. Two analog signals from the SLSG in a scanning mode (up/down channel output of the position amplifier and TTL synchronizing output of the scanner) were each sampled at a frequency of 25 kHz for 30–90 s. Typical samples of simultaneous time series of the VV, HH, SLSG (without scanning), and wire gauge signals, taken in the first mode, are presented in Fig. 2(a) and (b). The data correspond to a case with a wind speed of 5 m/s and a 6° grazing angle for upwind [Fig. 2(a)] and downwind [Fig. 2(b)] directions of illumination. Patches of spiky and high-frequency waves both for the SLSG time series and the scattered signal (especially HH upwind) are to be noted. The random character of the signals restricts the possibility of a deterministic analysis of the data; thus, different types of statistical analysis were used.

F. Scattered Signal Processing

Processing of the scattered signal was described in detail in [14]. The amplitude (power) and phase (frequency) parameters of the scattered signal were calculated separately, using only the in-phase components for VV and HH. For the power, the HH and VV signals were detected and low-pass filtered at $F_c = 50$ Hz to remove phase fluctuation. The resulting magnitude (power envelope) was converted to a cross-section per-unit area σ_o, using calibration data. To obtain mean Doppler spectra from the HH and VV signals, 2048-point fast Fourier transforms (FFT's) were performed with a frequency resolution of 0.4 Hz. Note that the Doppler spectrum includes both phase and amplitude fluctuations. A comparison with spectra of phase fluctuations only, obtained from both in-phase and quadrature signals, was made. It was found that the influence of the amplitude fluctuation is negligible in the frequency range of interest.

For kinematic considerations, the frequency (velocity) parameters of the scattered signal, as well as the short wave characteristics, should be presented in terms of the local phase of the dominant wind waves. To obtain local spectra, the full 5-min time series were divided into 0.25–0.375-s windows with 0.125-s overlap. For each window, FFT's were performed with a frequency resolution of 3–4 Hz.

G. SLSG Signal Processing

To obtain the 2-D wavenumber-frequency spectrum $S(\omega, k)$, as well as local values of the phase velocity, frequency, and wavelength of the short gravity-capillary waves, 2-D space-time SLSG data were used. Since the SLSG was scanning along the channel, the X-axis, k is the along-channel wavenumber component. An example of such a space-time X-T picture as well its cross section in the X and T directions are shown in Fig. 3 for a moderate wind speed of 5 m/s. The full time period (from trough through crest to trough) of a dominant wind-wave fragment was chosen. The presence of short waves in the frequency range 15–30 Hz (T-section) and wavelength range of 0.5–5 cm (X-section) can be seen. A projection of this data on the X-T plane for several dominant wave periods is shown in Fig. 4(a). The white areas correspond to regions of higher slope consistent with the forward face of a dominant wave ($F_o = 2$ Hz). Here the presence of patches of very short high-frequency waves in areas associated with the dominant waves is clear. A remarkable feature of these bound waves is that their phase velocity is equal to the phase velocity of the dominant waves. These waves are responsible, as will be shown later, for a significant part of the backscattering and therefore, require special attention.

H. Filtering

At first, 2-D frequency-wavenumber $(\omega - k)$ filtering with different 2-D bands to emphasize the differences between normal free waves, which correspond to the linear dispersion relation, and bound waves, was used. The examples of this procedure are presented in Fig. 4(b)–(d). Fig. 4(b) shows the result of using a 2-D filter with narrow bandwidth in the k-space ($k_o = 1$ cm^{-1}, which is close to the value of the k-Bragg component of our Ku-band scatterometer) and broad in ω ($F = \omega/2\pi = 10$–100 Hz).

The filtered image [Fig. 4(b)] has several noteworthy features. It consists of a sequence of interlaced patches with different frequencies and phase velocities. One group of patches has smaller phase velocities appropriate to free surface waves, while the second with higher phase velocities, corresponds to

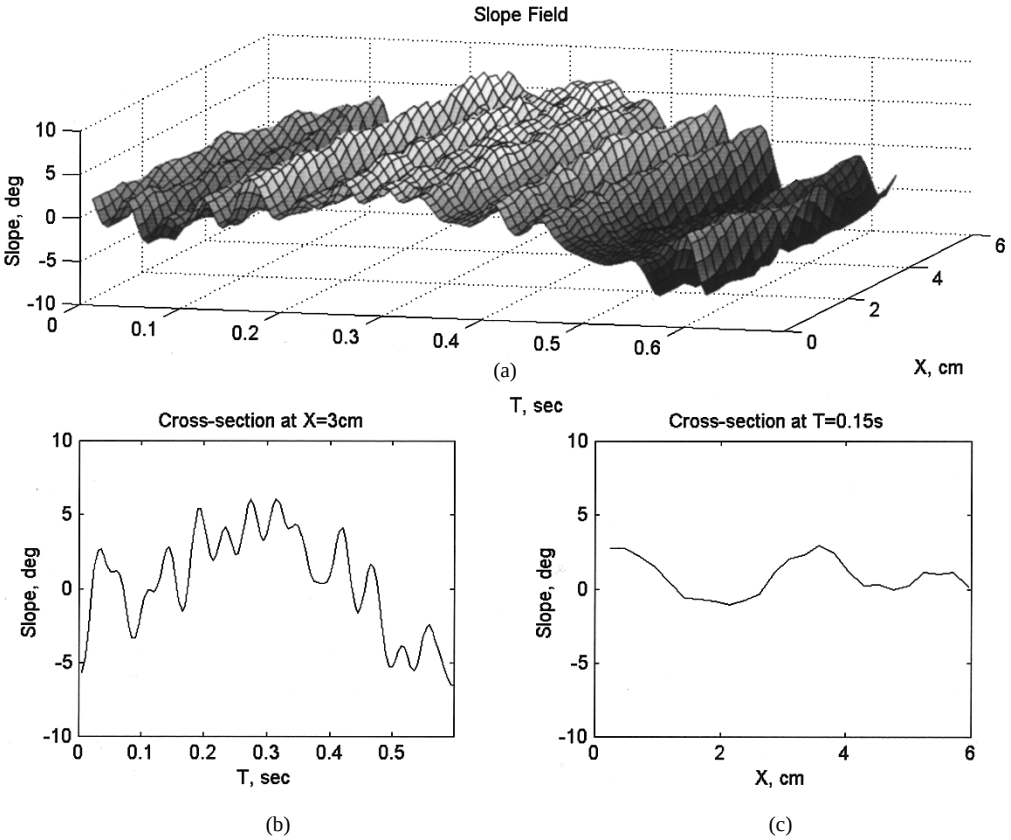

Fig. 3. Delft: a sample of the slope field in (a) space time and its cross section in the (b) T and (c) X direction ($U = 5$ m/s).

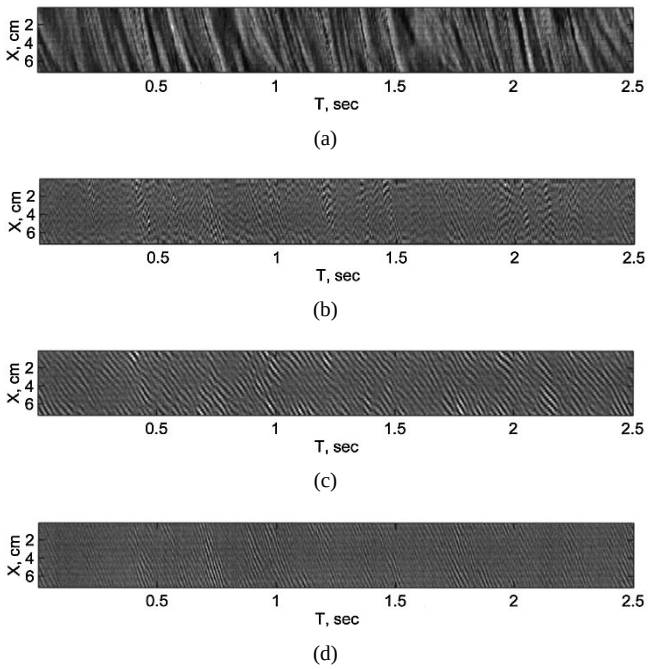

Fig. 4. Delft: the image of the slope (a) without filtering, (b) band-pass-filtered with $k_o = 1$ cm^{-1} and broadband ($F = 10$–100 Hz), (c) narrow band with $F_o = 40$ Hz, and (d) narrow band with $F_o = 70$ Hz.

bound waves. To emphasize the differences between the free and bound waves, additional filtering with the same k_o, but with a low-frequency band ($F_o = 40$ Hz) for the free waves, and a high-frequency band ($F_o = 70$ Hz) for the bound waves (with $\Delta F/F_o$ fixed), was done [Fig. 4(c) and (d)]. Fig. 4(c) shows that the main part of the free-wave area is coincident with the troughs of the energy-containing waves, while in Fig. 4(d) the bound waves are predominantly near the crests of the dominant waves.

Two-dimensional local wavenumber-frequency spectra, taken with a 7-cm/0.1-s 2-D window (with 0.05-s overlap) for the same space-time series, are shown in Fig. 5. Despite the small confidence intervals for the spectral estimates, the variation of $S(F, k)$ from spectrum to spectrum can be seen, as the local spectra are modulated with the phase of the dominant long waves. A modulation of short free waves by the orbital motion of the dominant waves, or the presence of high-frequency bound waves, could produce these phenomena and will be discussed in detail below.

An example of using a spectrogram to define the phase velocity field of capillary waves of fixed wavenumber along the dominant long waves is presented in Fig. 6. Here the spectrogram $S(C, T; k_o)$ for the fixed k_o component with a wavelength of 2 cm is interpreted as a function of the phase velocity C in Fig. 6(a). To obtain such a picture, the initial X-T data of 6-s duration was 2-D filtered (from 5–150 Hz in frequency and from 0.25 to 0.75 cm^{-1} in wavenumber), and then the spectrogram for the X cross section (the window is 0.1 s with 0.05-s overlap) was taken.

I. Bispectral Analysis

We now use the bispectrum and bicoherence as a measure of coupling between surface gravity waves and small capillary waves bound to the dominant long waves. The interpretation of

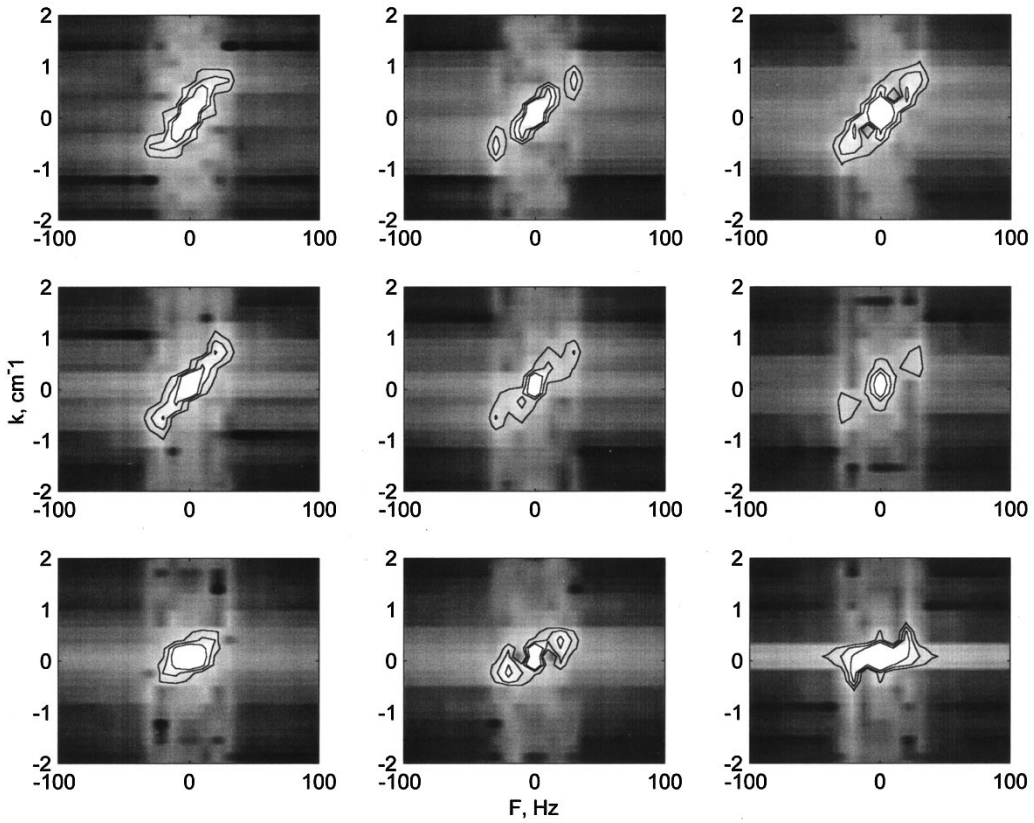

Fig. 5. Delft: local $S(F, k)$ slope spectra with 0.1-s window and 0.05-s overlap, corresponding to space-time series in Fig 4(a) (from left to right and top to bottom).

the bicoherence varies depending on the type of signal under study [3]. For a stochastic signal, such as the wave slope in wind-driven waves, the amplitude of the bicoherence gives a measure of the signal skewness.

The estimate of the bispectrum is computed by dividing the laser-slope-gauge time series of length N into K segments, each of 1000 point length. An 1000-point FFT is performed on each segment to give $X_i(f_1)$, $(i = 1, 2, \cdots, K)$, and the raw bispectral estimate $B_i(f_1, f_2) = X_i(f_1)X(f_2)X_i^*(f_1 + f_2)$ is averaged over all segments [7]

$$\hat{B}(f_1, f_2) = \frac{1}{K}\sum_{i=1}^{K} X_i(f_1)X(f_2)X_i^*(f_1 + f_2). \qquad (2)$$

It is common to normalize the estimate in (2) to form the bicoherence function $b(f_1, f_2)$. In this paper, the bicoherence is considered because it has the attractive property of being bounded between zero and one [2]. The bicoherence $b(f_1, f_2)$ is defined by the following expression:

$$\hat{b} = \frac{\left|\sum_{i=1}^{K} X_i(f_1)X(f_2)X_i^*(f_1 + f_2)\right|}{\left(\sum_{i=1}^{K}|X_i(f_1)X(f_2)|^2\right)^{1/2}\left(\sum_{i=1}^{K}|X_i(f_1 + f_2)|^2\right)^{1/2}}. \qquad (3)$$

The main results of such an analysis are given in the next section.

III. Results

Let us first consider the features of the scattering water surface, then the characteristics of the scattered signal.

A. Wave Field Parameters

1) Surface Wave Height Spectra: To underline the features of the Delft channel with a large fetch, let us compare the Delft channel wave data with those taken in the SIO channel [14] under similar wind conditions. Typical samples of spectral estimates of time series from a single wave gauge for different wind speeds from 2.5 to 12.5 m/s in both channels are presented in Fig. 7(a). While the high-frequency parts of each pair of spectra are similar, due to the different fetches, we can see a large difference in the dominant waves. The values of peak frequency F_o, as well as calculated values of the orbital velocity for these waves, are presented for both channels in Fig. 7(c) and (d), where significant differences between parameters of the dominant waves are apparent between the two channels. Thus, it should not be surprising if different scattering phenomena contribute differently in the two channels. This will be considered in the next section.

A more detailed comparison of the high-frequency parts of the spectra requires suitable scaling and nondimensionalization of the spectra. Fig. 8 shows the nondimensional spectra $S'(F') = S(F/F_o)F^4/[S(F/F_o)F^4]_{1.5-3}$, where F' is nondimensional frequency F/F_o and $[S(F/F_o)F^4]_{1.5-3}$ is the mean value of the spectral density $S(F/F_o)F^4$ in the

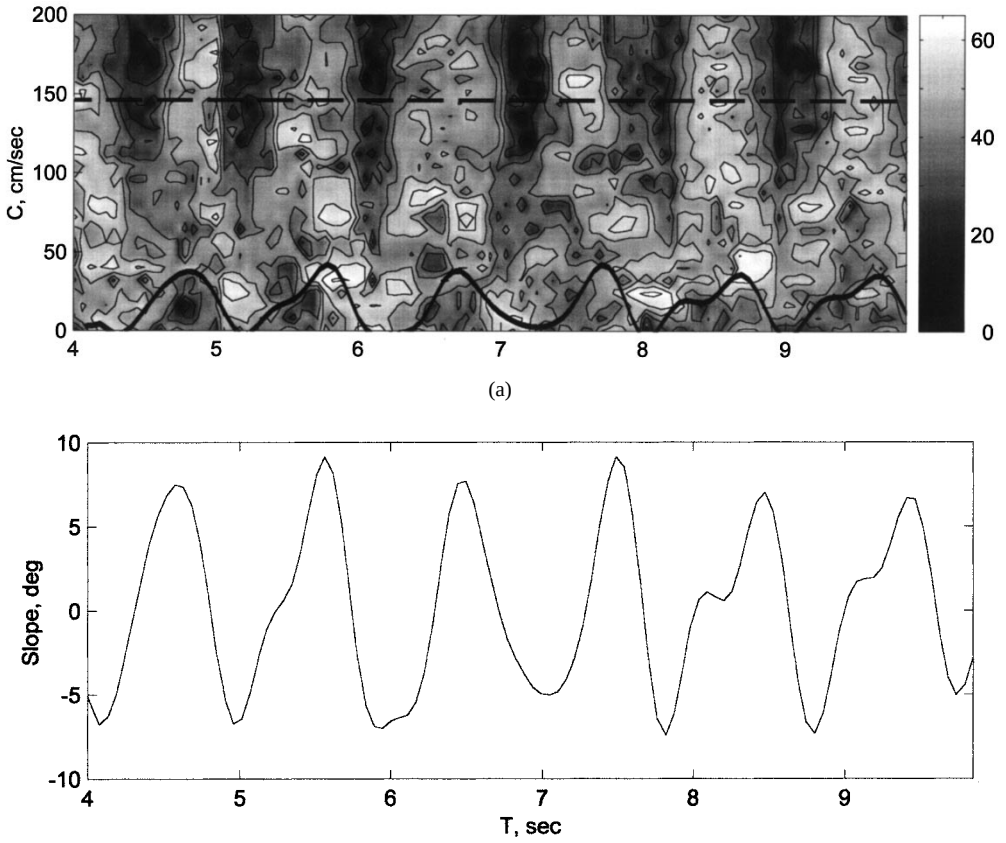

Fig. 6. Delft: $S(C, k_o, T)$ spectrogram for $k_o = 0.5$ cm^{-1} in terms of the (a) phase velocity and (b) corresponding mean slope time series. Calculated values of C_o of the dominant waves—dashed line; $V_{orb} + U_d$—solid line.

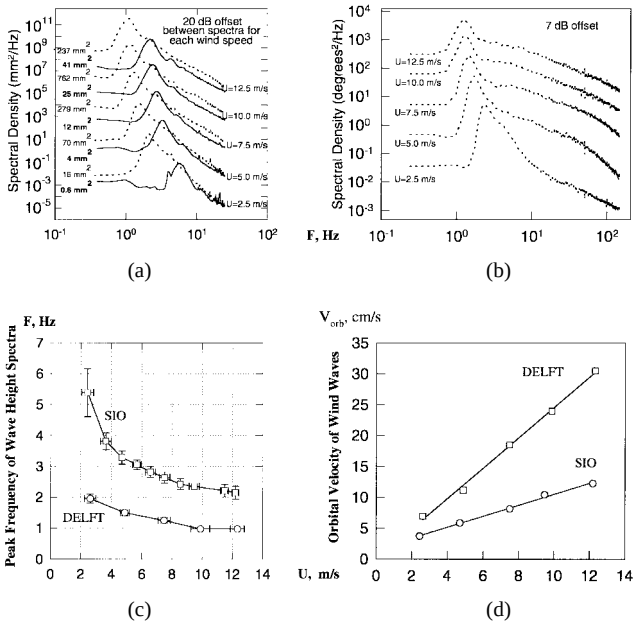

Fig. 7. Typical (a) wave height and (b) wave slope spectra for different wind speeds (—SIO, ··· DELFT). Dependence of the peak frequency of the (c) wave spectra and (d) orbital velocity of dominant waves on wind speed. Note that the difference in the fetch (80 m for DELFT and 11 m for SIO) causes a large difference in the dominant waves in the channel.

frequency range F/F_o between 1.5 and 3. The high-frequency spectra are similar for both channels at the higher wind speeds: 7.5–12.5 m/s.

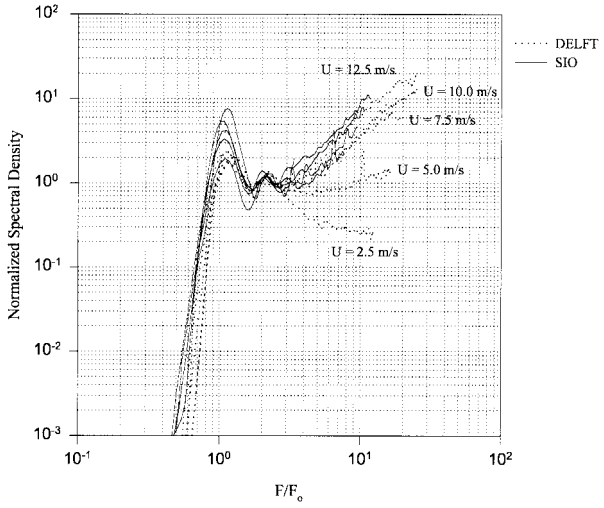

Fig. 8. Nondimensional smoothed wind-wave spectra for SIO and Delft channels. Note the similarity of the high-frequency parts of the spectra for both channels at high winds.

2) Surface Wave Slope Spectra: Let us now consider spectra of the time series from the SLSG without scanning. Examples of wave slope spectra for five wind speeds in the Delft channel from 2.5 to 12.5 m/s are presented in Fig. 7(b). The presence of high-frequency (capillary) waves up to 150 Hz is clear for winds greater than 2.5 m/s. It should be mentioned that free and bound wind-generated waves cannot be distinguished in a 1-D frequency spectrum.

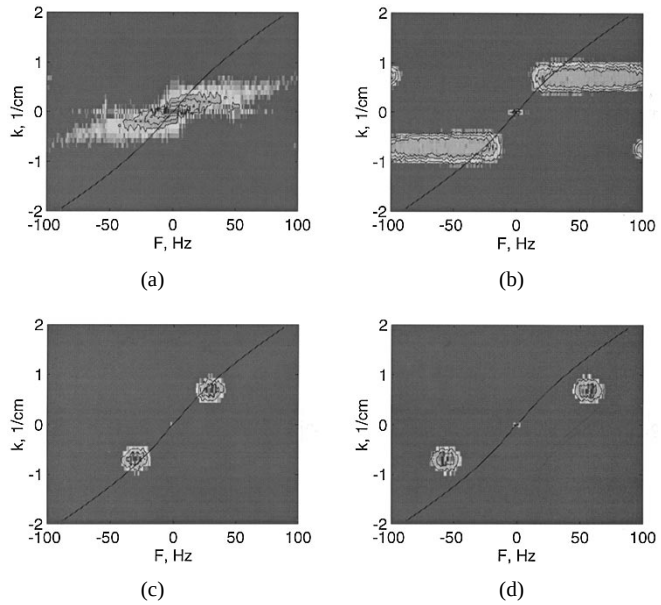

Fig. 9. Delft: 2-D wavenumber frequency spectra corresponding to the space-time series in Fig. 4(a)–(d). Note the significant values of spectral density in the high-frequency area related to bound waves.

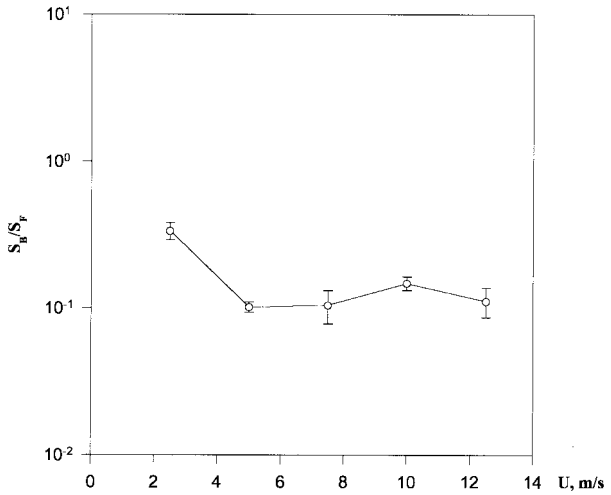

Fig. 10. Delft: ratio of the spectral density $S_B(F_B)/S_F(F_F)$ of the bound and free-wave slopes. Frequencies F_B and F_F correspond to calculated values of slow and fast scatterers in the Doppler spectra.

Two-dimensional spectral analysis, which can resolve the differences in the phase velocities, can accomplish this goal. These methods were demonstrated in Section II-G (see Fig. 4).

Now, 2-D wavenumber-frequency $S(k_x, F)$ spectra, which correspond to the space-time series in Fig. 4, are shown in Fig. 9, as follows:

1) 2-D spectrum without filtering;
2) fixed k_o with F_o in the range 10–100 Hz;
3) free waves ($F_o = 30$ Hz);
4) bound waves ($F_o = 70$ Hz).

The linear dispersion relation $F(k)$ is also shown in each frame. The bound waves do not satisfy the linear dispersion relationship for free surface waves, and their energy density is not negligible when compared to that of the free waves. They are located in the areas with the higher phase velocities. It should be remembered that only the along-channel component of the slope field was measured and no information regarding the directional-frequency spectrum $S(\Theta, F)$ or 2-D wavenumber spectrum $S(k_x, k_y)$ was obtained. The finite width Θ_o of the directional-wavenumber $S(k_x, k_y)$ spectra needs to be taken into account. Such spreading would cause a slight shift in the values of the measured $S(k_x, F)$ spectra toward lower phase velocities (frequencies). A quantitative comparison of the ratios of spectral density $S_B(F_B)/S_F(F_F)$, obtained from 2-D spectra $S(k_o, F)$ [see Fig. 9(c) and (d)] versus wind speed, is shown in Fig. 10. Frequencies F_b and F_f correspond to the centers of these areas in Fig. 9(c) and are consistent, as will be shown below in Section III-B, with calculated values of F_{o_s} ("slow" scatterers) and F_{o_f} ("fast" scatterers) of the Doppler spectra.

3) Bispectral Analysis: This method was applied for the calculation of the bicoherence of the SLSG time series for five different winds in the range 2.5–12.5 m/s. The amount of available data for bispectral analysis includes 120 000 points for 2.5 m/s, 180 000 points for 5 m/s, 420 000 points for 7.5 m/s, 660 000 points for 10 m/s, and 1 320 000 points for 12.5 m/s. We have previously noted that Fig. 7(b) presents the original laser-slope-gauge data for the five winds. As illustrated in Fig. 7(c), the spectral maximum for the light winds (2.5 and 5 m/s) is about 2 Hz, while the spectral maximum for higher winds is close to 1 Hz. It is evident from (3) that the bicoherence has two independent frequency axes f_1 and f_2 and that the bicoherence magnitude emerges from the frequency plane. In Fig. 11, we demonstrate a small region of the f_1, f_2-plane for the experiment with wind speed 5 m/s. A peak in the bicoherence magnitude of this data set occurs at frequencies approximately $f_1 = 2$ Hz and $f_2 = 50$–150 Hz. The peak in the bicoherence is about 0.5, with small bicoherence amplitude (0.1–0.2) at other frequencies.

If the bicoherence has a value of f_2, a nonlinear interaction exist between given frequencies; otherwise (bicoherence is equal to zero), there is no interaction. That is, the bicoherence for the sum interaction was 0.5 (Fig. 11), which implies that only half of the power at f_1 is due to the interaction of the high frequency waves at f_2 from 50 to 150 Hz.

Fig. 12(a)–(c) are summary bicoherence plots for all wind data sets and were smoothed with a 40-Hz window. Cases (a)–(c) correspond to cuts parallel to the f_2-axis for f_1 equal to 1–3 Hz, respectively. The maximum amplitude of the bicoherence depends on the wind speed. The bicoherence cross section through the 1-Hz component shows a maximum for a wind speed of 7.5 m/s, while the peak of bicoherence at cross sections through the 2- and 3-Hz components occur at 5 m/s. The positions of these maxima (Fig. 12) indicate an interaction in the system of gravity-capillary waves, resulting in the formation of higher frequency capillary waves.

B. Scattered Signal Parameters

The main goal of this study was to understand how the presence of both free and bound waves could affect the electromagnetic scattering. Thus, of particular interest are the characteristics of the scattered signals and the wave field,

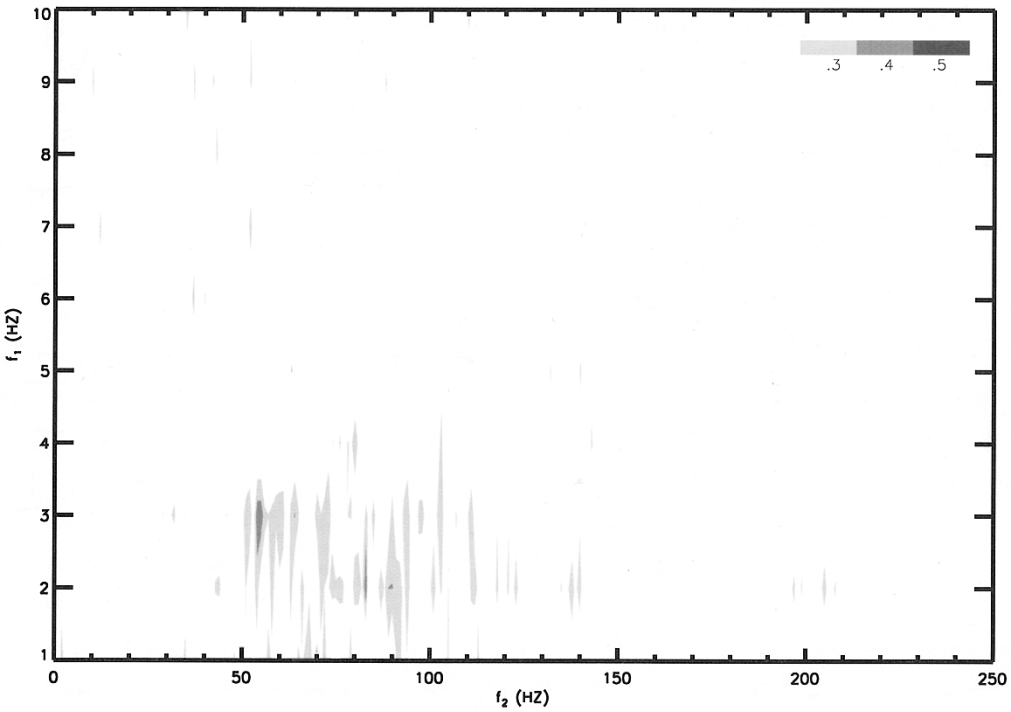

Fig. 11. Delft: contours of bicoherence of the LSG time series at wind speed 5 m/s.

which can be associated with the kinematics, i.e., the electromagnetic Doppler spectra and the phase velocities of the different parts of the surface wave field. The amplitude parameters of the scattered signals (absolute cross section), which were defined separately, will also be presented.

1) Doppler Spectra: Fig. 13 represents several samples of Doppler spectra for the typical experiments at 6° grazing angle, downwind direction of illumination, VV and HH polarizations, in both wind-wave channels. Each spectrum is narrow with one significant peak. With wind speed increasing from 2.5 to 7.5 m/s, the spectra become broader and the peak frequencies shift due to the increasing wind-drift velocity. The positions of the peak are in agreement with calculated values of the frequency of Bragg components for free waves. The small differences between the peak frequencies of the Doppler spectra for the different wave channels are due to the smaller wind-drift velocity in the Delft channel, which has a deeper wind-tunnel section. Shadowing effects, which will be discussed later, may also contribute to this difference.

A different picture emerges in Fig. 14 for the upwind direction of illumination. The Doppler spectra for HH polarization and wind speeds 5 and 7.5 m/s become bimodal, and the energy density in the second (higher-frequency) peak grows with increasing wind speed. The values of F_o for the first (lower-frequency) peak are close to the corresponding values for the downwind direction and are consistent with the Bragg scattering from free waves. At the same time, second peak for all HH Doppler spectra in the upwind direction of illumination corresponds, as will be shown below, to Bragg-scattering from bound capillary waves. While the energy density of the second peak for the SIO data is dominant, except at the lowest wind speed, the Delft data have a stronger bimodal structure.

2) Peak Frequency of Doppler Spectra: The bimodal structure of the Doppler spectra is evident (especially for Delft HH), though the energy distribution between low- and high-frequency parts of the spectra depends strongly on the experimental conditions. For some estimates, it is useful to simplify the procedure and use the peak frequency of the mean Doppler spectrum. The polarization difference, for example, can be seen quite clearly in the dependence of the peak frequency of the Doppler spectrum on wind speed.

Fig. 15 shows several samples of mean Doppler spectra for the typical SIO (left) and Delft (right) experiment at 6° grazing angle, for upwind illumination and both VV and HH polarization. The corresponding wave height spectra for these wind speeds of 2.5 to 12.5 m/s are shown in Fig. 7(a). Estimating peak values of F_o for all SIO spectra is a relatively simple procedure, with the observed peak Doppler frequencies reflecting features of the HH upwind "fast" scatterers [14].

The corresponding procedure for estimating the Delft data however is not so simple. Each Delft spectrum contains two very broad low- and high-frequency parts; for some spectra, the position of the peak value F_o of these parts is difficult to quantify. Broadening of the mean Doppler spectra is due to modulation by the orbital velocity of the dominant wind waves, which is a larger effect for the Delft data. Fig. 16 presents averaged data for $F_o(U)$ dependence for all experiments in the both channels (see Table I). It is clear that the case for HH and upwind illumination has a different character in comparison with all other situations (a higher value of F_o) and may be considered as evidence of scattering from the bound waves. Some significant differences between SIO and Delft values (for VV especially) can be noticed due to the influence of long waves and will be discussed in detail below.

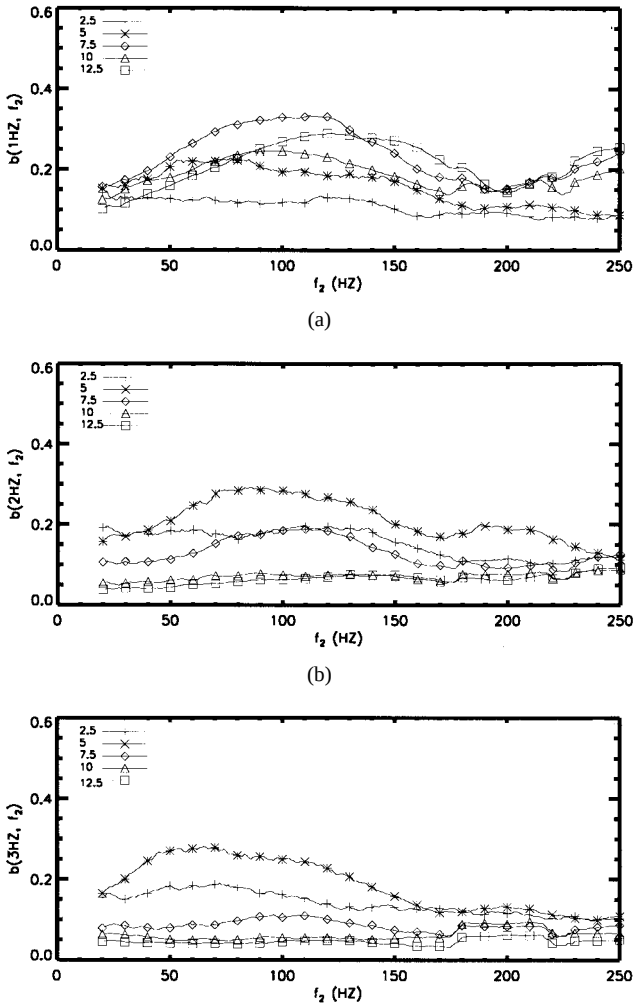

Fig. 12. Delft: cross section of the bicoherence spectra smoothed with a 40-Hz window for frequencies (f_1): (a) 1 Hz; (b) 2Hz; (c) 3Hz, and for all winds.

3) Absolute Cross Section: The previous description of the Doppler characteristics suggests the presence of two different sources of scattering. The scattered power measured by the absolute cross section might also show evidence of different types of scatterers. Note, however, that measurement of the absolute cross section is more error-prone than measurement of the Doppler spectra. In particular, in order to estimate absolute cross section, the entire Doppler spectra over all frequencies should be integrated. Fig. 17(a) and (b) shows the dependence of the cross section σ_o on the wind speed U for a 6° grazing angle, in both upwind and downwind illumination for both wave channels. The similarity between SIO and Delft data and the monotonic increase of σ_o with wind speed for downwind illumination is clear: σ_{VV} exceeds σ_{HH}, and the VV/HH polarization ratio is approximately 10–15 dB, as expected. However, Fig. 17(a) for upwind illumination displays some interesting features for the SIO data, which may be interpreted as an indication of the presence of two sources of backscattering [14]. For Delft data no significant differences between upwind and downwind direction of illumination were observed.

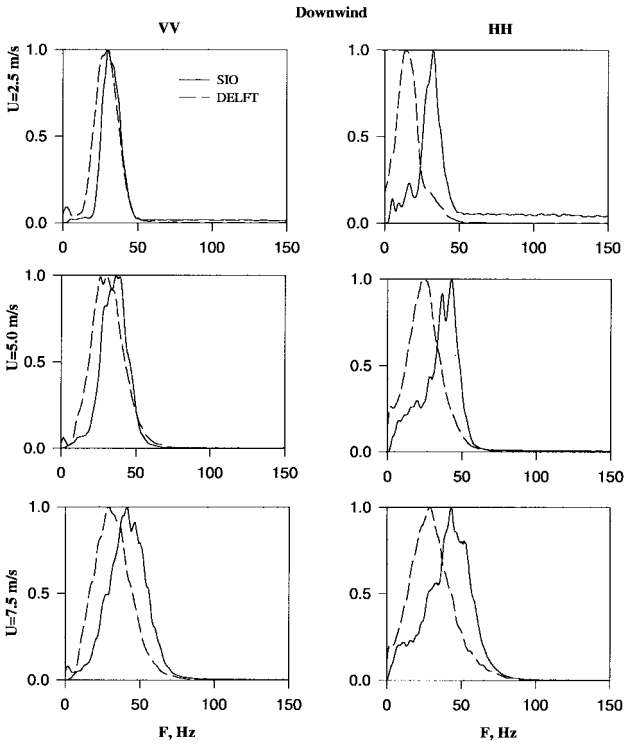

Fig. 13. Comparison of the Doppler spectra for downwind look direction, a 6° grazing angle, and various wind speeds. All spectra are consistent with Bragg scattering from free capillary waves. Peak frequency of spectra obtained at SIO are slightly higher due to higher wind-drift velocity.

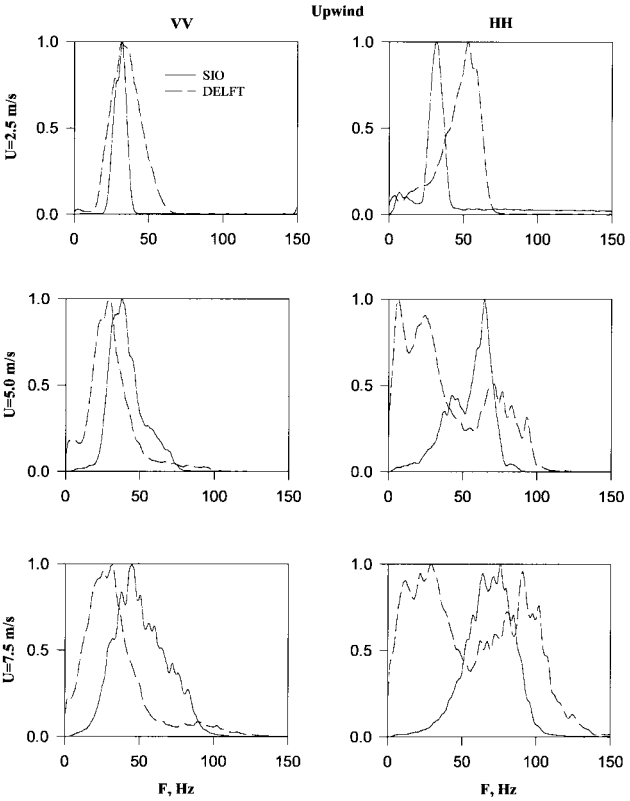

Fig. 14. Similar to Fig. 13, but for upwind look direction. Note the appearance of a high-frequency area for the HH-polarization, which is consistent with scattering from bound capillary waves.

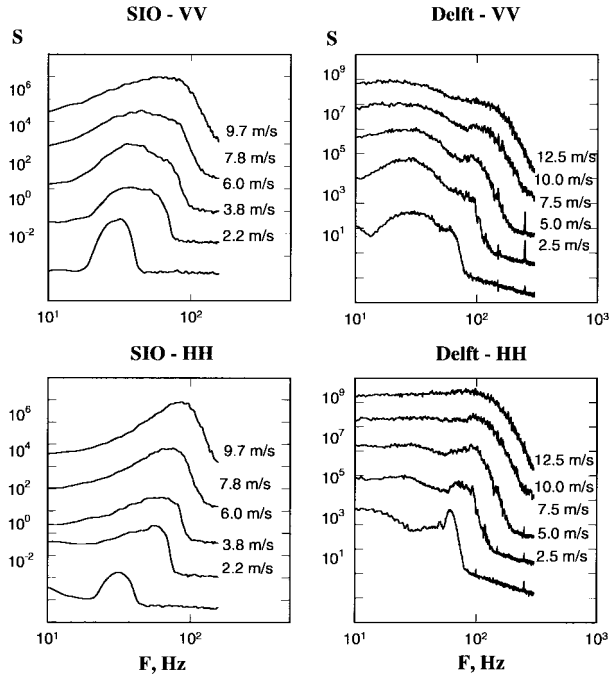

Fig. 15. Samples of mean Doppler spectra for VV and HH, upwind direction of illumination, and a 6° grazing angle for the both channels.

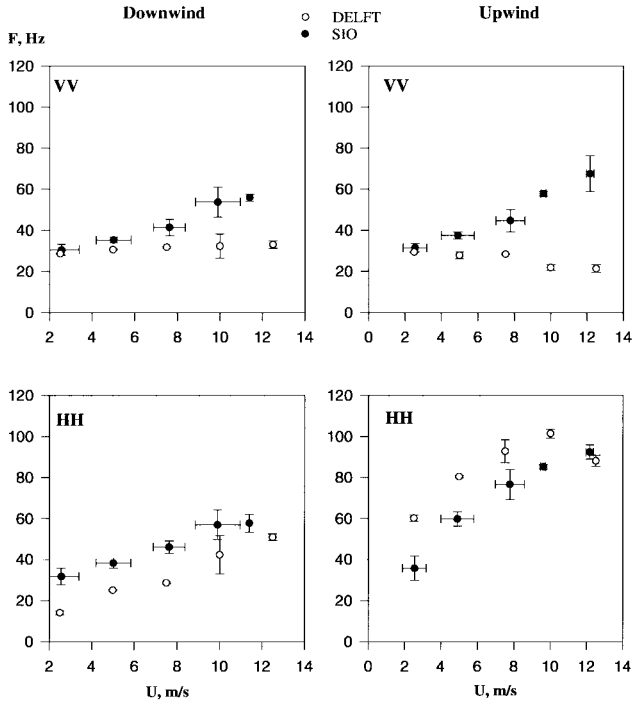

Fig. 16. Comparison of the dominant peak frequency of Doppler spectra F_o versus wind speed for different polarization, illumination directions, and a 6° grazing angle. The difference in wind-wave conditions for the two channels (smaller wind drift velocity and higher velocity of bound waves for the Delft facility) accounts for the differences in the measured data.

4) Grazing Angle Dependence: The analysis of the Delft channel data obtained for two grazing angles, 6 and 25°, reveals an absence of any significant influence of the grazing angle for both peak Doppler frequency and absolute cross section. The SIO channel data obtained at 6, 8, and 12° also show no significant differences in absolute cross section or peak Doppler frequency versus wind speed for both VV, HH, and upwind and downwind direction of illumination [14].

TABLE I
SUMMARY OF EXPERIMENTAL CONDITIONS

	Wind Speed	Number of Trials			
		Grazing angle 6°		Grazing angle 25°	
	m/s	Upwind	Downwind	Upwind	Downwind
DELFT	2.5	6	8	1	1
	5	4	8	1	1
	7.5	5	8	1	1
	10	4	8	1	1
	12.5	5	8	1	1
SIO	2	4	4	2	2
	4	5	4	2	2
	6	4	5	3	2
	8	6	4	2	2
	10	4	4	2	2
	12	2	3	1	2

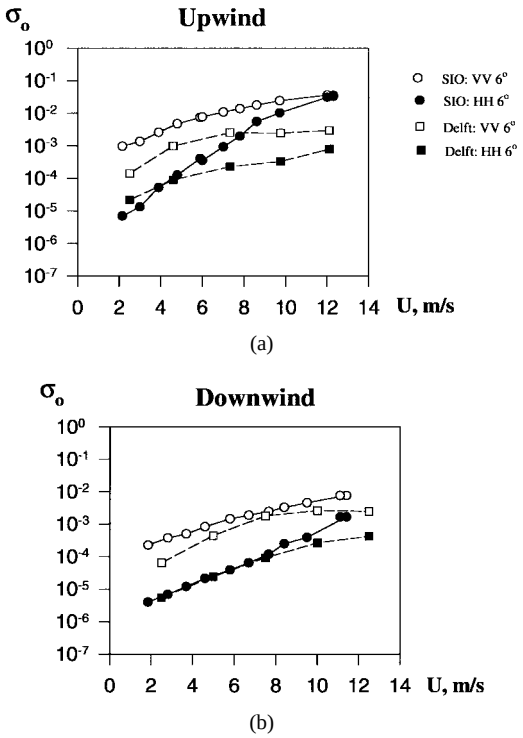

Fig. 17. Comparison of the mean cross section per unit area σ_o versus wind speed for in Delft and SIO channels for (a) upwind and (b) downwind direction of illumination.

IV. DISCUSSION

The presence of two different types of surface capillary waves, free and bound, is evident in the Delft wave data. Many authors have mentioned bound waves as a possible source of microwave scattering, but only by the use of high-frequency/high-wavenumber measurements in space-time can these waves be separated from free capillary waves having the same wavenumbers but different phase velocities. Bispectral analysis is also a useful tool for demonstrating the coupling between the lower frequency waves and the higher frequency

parasitic-capillary waves. One goal of separating the free and bound waves is the estimation of the energy density for both types of waves.

Determining how both types of small capillary waves can alter the surface scattering properties is not so clear. The study in the SIO channel of the amplitude and frequency characteristics of microwave scattering for different polarization and directions of illumination distinguishes two separate groupings of the backscattered data. The first group corresponds to HH scattering in the upwind direction, and the second corresponds to HH scattering in the downwind direction and all VV scattering. These groups may be associated with different scattering mechanisms. The second grouping is considered to be associated with Bragg scattering from free capillary wind waves, while the first was interpreted as scattering from the bound capillary wind waves. As has been shown in [14], such a separation is consistent with estimates of the phase velocities of the different types of capillary waves.

We now consider a similar grouping of the Delft data, taking into account the different wind-wave conditions in both wind-wave channels. Results of this kinematic comparison are presented in Fig. 18 for the Delft and SIO channels. Here the phase velocities for different types of wind-waves are estimated as a functions of wind speed. For the measured values of phase velocity, the peak frequency of each Doppler spectrum is converted to velocity using the Doppler conversion of 94 Hz per m/s.

The phase velocity is estimated by

$$C = C_o + U_d \pm V_o; \qquad U_d = 0.03U \tag{4}$$

where U_d is the wind drift current at the water surface, V_o is the horizontal component of orbital velocity of the dominant waves, and C_o is the phase velocity based on the dispersion relation for gravity-capillary waves

$$C_o = \frac{\omega}{k} = \sqrt{\frac{g}{k} + \frac{Tk}{\rho}}. \tag{5}$$

Here ω is the angular frequency of surface waves, taken from the peak frequency for the dominant wind waves or Bragg resonant frequency for the capillary waves, k is the wavenumber of the surface waves, g is the acceleration of gravity, T is the surface tension, and ρ is the water density.

For shallow water, the horizontal component of orbital velocity V_o can be defined as

$$V_o = -\frac{H\omega}{kd}\cos(\omega + kx) \tag{6}$$

where H is the waveheight, ω is the angular frequency ($\omega = 2\pi F$), k is the wavenumber of the long waves, and d is the water depth. The large difference between values of V_o for Delft and SIO should be noted [see Fig. 7(d)].

We first consider the results for the SIO channel [Fig. 18(b)]. There is agreement between the measured data and the calculated Doppler frequencies based on the surface wave data at all wind speeds. Note the agreement between measured HH upwind and curve 1 (phase velocity of dominant or bound waves), as well as the rest of the measured data and curve 3

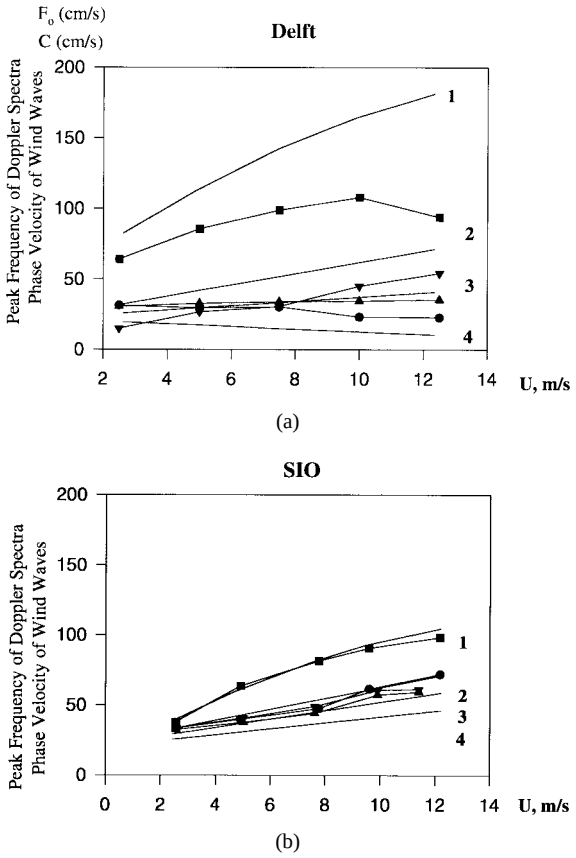

Fig. 18. Comparison of different types of scatterers and dependence of different scatterers on the wind speed for (a) Delft and (b) SIO for a 6° grazing angle. Measured Doppler: • VV Up, ■ HH Up, ▲VV Down, ▼HH Down. Calculated curves: 1–Phase velocity of bound waves. 2–Phase velocity of free waves on crest. 3–Phase velocity of free waves. 4–Phase velocity of free waves on troughs.

(phase velocity of free Bragg waves) or curve 2 (phase velocity of the free Bragg waves on the crest of dominant wind waves).

Now we consider the Delft data, in which a grouping like that for the SIO data, albeit with larger scattering, may be proposed. Again, the measured HH downwind data and data for both VV illuminations may be compared to curve 3 (phase velocity of free Bragg waves). However, the measured HH upwind Doppler frequencies are less than the calculated values of phase velocity of bound waves based on the peak of the wave spectrum.

The most likely reason for such a discrepancy is the spatial resolution of our scatterometer (45 cm), which is not small compared to the wavelength of the dominant waves (wavelength 40–160 cm). The measurements with ultrahigh spatial resolution [17] have found strong localization of the different kinds of scatterers. In a recent study in the SIO channel with the same Ku-band scatterometer, but with much larger regular long waves (wavelength 6 m), the presence of free waves on the troughs and bound waves on the crests of the long waves was observed [15]. Spatial smoothing might affect the separation of low- and high-frequency parts of the Doppler spectra and should be taken into account in interpreting the Delft data. Nevertheless, the grouping is similar for both channels, with 15–30% differences in the mean values of

the peak Doppler frequencies F_o inside each group. One difference for Group I (bound waves) is obvious, with the phase velocity of dominant waves (bound waves) being higher for the Delft at the same wind speed than for SIO. As far as Group 2 (free waves), all SIO data form a compact group in the neighborhood of F_o, rising slightly due to increasing wind drift. At the same time, the Delft $F_o(U)$ dependence surprisingly stays steady (with some small trend for different polarization and look direction). Note that the dominant wave parameters remain steady with increasing wind. The smaller wind drift velocity for Delft due to the larger size of the channel height and the presence of some counter current might also explain the observed features.

Let us finally clarify the nature of the scattering mechanism from bound capillary waves. While the Bragg scattering phenomenon is evident in the case of free capillary waves, it is not so obvious for bound waves. Indeed, parasitic-capillary waves may be strongly nonlinear and the method of small perturbations may not be valid for calculation of the scattered field.

To better understand the features of scattering from steep bound waves, in the SIO glass laboratory wave channel scattered signals at grazing incidence from steep mechanically-generated (3–6 Hz) waves, and wind waves, and the fine space-time structure of the surface have been measured [12], [16]. It was found that Doppler spectra of the scattered signal are consistent with Bragg scattering from bound capillary waves generated by the dominant waves.

V. Conclusions

Laboratory measurements of Ku-band scattering at grazing incidence, as well as fine space-time measurements of wind waves in the SIO and Delft Hydraulics Laboratory wind-wave channels are presented. This study was stimulated by the need to identify the processes that significantly contribute to scattering at grazing and moderate incidence angles.

Measurements of the Doppler frequency of the scattered signal showed that the Doppler spectra may have a bimodal structure. The low-frequency peak of the spectrum corresponds to Bragg scattering from free capillary waves (slow scatterers), while the high-frequency part is clearly associated with Bragg scattering from the bound capillary waves on the crests of the steeper wind waves (fast scatterers).

The distribution in the Doppler spectra for these types of scattering is approximately equal and depends on the geometry of the illumination and the wind condition. For the upwind direction of illumination and HH polarization, fast scattering is predominant.

Classification of the scattered signal by separation into free and bound Bragg scatterers is kinematically consistent with direct measurement of the parameters of the small wind waves responsible for the scattering. A study of space-time structure of these waves demonstrates the presence of two different types of capillary waves: free and bound. Two-dimensional filtering was used to separate free and bound surface waves. While the phase velocity of the free waves is in an agreement with the dispersion relation for surface gravity-capillary waves, the phase velocity of bound waves is equal to the phase velocity of the steeper wind waves.

Bispectral analysis of the wave-slope data shows that there are nonlinear interactions between the dominant wind waves and the higher-frequency gravity-capillary and capillary waves.

Acknowledgment

The authors would like to thank D. Quigley for his active participation in all stages of measurements and data processing. The authors also wish to thank their colleagues at the Hydraulics Laboratories in Delft and Scripps Institution of Oceanography for their assistance.

References

[1] J. Chang, R. Wagner, and H. Yuen, "Measurement of high frequency capillary waves on steep gravity waves," *J. Fluid Mech.*, vol. 86, no. III, pp. 401–413, 1978.
[2] S. Elgar and R. T. Guza, "Statistics of bicoherence," *IEEE Trans. Acoust., Speech, Signal Processing*, vol. 36, pp. 1667–1668, 1988.
[3] ——, "Nonlinear model predictions of bispectra of shoaling surface gravity waves," *J. Fluid Mech.*, vol. 167, pp. 1–18, 1986.
[4] T. Hara, E. J. Bock, and D. Luzenga, "*In situ* measurements of capillary-gravity wave specta using a SLSG and microwave radars," *J. Geophys. Res.*, vol. 99, no. 12, pp. 593–612, 1994.
[5] T. Hara, E. J. Bock, and M. Donelan, "Frequency-wavenumber spectrum of wind-generated gravity-capillary waves," *J. Geophys. Res.*, vol. 102, no. C1, pp. 1061–1072, 1997.
[6] M. Keller, R. B. Cotwols, W. J. Plant, and W. C. Keller, "Comparison of optically-derived spectral densities and microwave cross sections in a wave-wind tank," *J. Geophys. Res.*, vol. 100, no. 16, pp. 163–216, 1995.
[7] Y. C. Kim and E. J. Powers, "Digital bispectral analysis and its applications to nonlinear wave interactions," *IEEE Trans. Plasma Sci.*, vol. PS-7, no. 2, pp. 120–131, 1979.
[8] D. S. W. Kwoh and B. M. Lake, "A deterministic, coherent, and dual polarized laboratory study of microwave backscattering from water waves—Part I: Short gravity waves without wind," *IEEE J. Oceanic Eng.*, vol. OE-9, pp. 291–308, Sept. 1984.
[9] B. K. Jahna and K. S. Riemer, "Two-dimensional wave number spectra of small-scale water surface waves," *J. Geophys. Res.*, vol. 95, no. C7, 11 531–11 546, 1990.
[10] M. S. Longuet–Higgins, "The generation of capillary waves by steep gravity waves," *J. Fluid. Mech.*, vol. 16, pp. 238–259, 1963.
[11] W. K. Melville, A. D. Rozenberg, and D. C. Quigley, "Bound capillary waves as microwave scatterers: A laboratory study," in *IGARRS 1995 Abstracts.*
[12] W. K. Melville, D. C. Quigley, M. J. Ritter, and A. D. Rozenberg, "A laboratory study of polarized microwave scattering from steep wind waves at grazing incidence," in *Proc. IGARRS 1997.*
[13] M. Perlin, H. Lin, and C. Ting, "On parasitic capillary waves generated by steep gravity waves: An experimental investigation with spatial and temporal measurements," *J. Fluid Mech.*, vol. 255, pp. 597–620, 1993.
[14] A. D. Rozenberg, D. C. Quigley, and W. K. Melville, "Laboratory study of polarized scattering by surface waves at grazing incidence—Part I: Wind waves," *IEEE Geosci. Remote Sensing*, vol. 33, pp. 1037–1046, Nov. 1995.
[15] ——, "Laboratory study of polarized scattering by surface waves at grazing incidence—Part II: The influence of long waves," *IEEE Geosci. Remote Sensing*, vol. 34, pp. 1331–1342, Nov. 1996.
[16] A. D. Rozenberg and W. K. Melville, "Laboratory study of microwave scattering from periodic bound parasitic capillary waves," *Amer. Geophys. Union 1996 Abstracts.*
[17] D. B. Trizna, J. P. Hansen, P. Hwang, and J. Wu, "Laboratory studies of radar sea spikes at low grazing angles," *J. Geophys. Res.*, vol. 96, no. C7, pp. 12 529–12 537, 1991.
[18] ——, "Ultra wideband radar studies of steep crested waves with scanning laser measurements of wave slope profiles," *Dyn. Atmos. Ocean.*, vol. 20, pp. 33–53, 1993.
[19] G. R. Valenzuela, "Theories for the interaction of electromagnetic and ocean waves—A review," *Boundary-Layer Meteorol.*, vol. 13, pp. 61–85, 1978.

[20] S. A. Yermakov, K. D. Ruvinsky, S. G. Salashin, and G. I. Friedman, "Experimental investigations of the generation of capillary-gravity ripples by strongly nonlinear waves on the surface of deep fluid," *Izv. Atmos. Ocean Phys.*, vol. 22, pp. 835–842, 1986.
[21] A. V. Fedorov and W. K. Melville, "Nonlinear gravity-capillary waves with forcing and dissipation," *J. Fluid Mech.*, vol. 354, pp. 1–42, 1998.
[22] A. V. Fedorov, W. K. Melville, and A. D. Rozenber, "An experimental and numerical study of parasitic capillary waves," *Phys. Fluids*, vol. 10, pp. 1315–1323, 1998.

Anatol D. Rozenberg, photograph and biography not available at the time of publication.

Michael J. Ritter, photograph and biography not available at the time of publication.

W. Kendall Melville, photograph and biography not available at the time of publication.

Christopher C. Gottschall, photograph and biography not available at the time of publication.

Andre V. Smirnov, photograph and biography not available at the time of publication.